

# Real-time probabilistic tsunami forecasting in Cascadia from sparse offshore pressure observations

Stefan Henneking<sup>1</sup>, Fabian Kutschera<sup>3</sup>, Sreeram Venkat<sup>1</sup>,  
Alice-Agnes Gabriel<sup>3,4</sup>, Omar Ghattas<sup>1,2</sup>

<sup>1</sup>Oden Institute for Computational Engineering and Sciences, The University of Texas at Austin

<sup>2</sup>Walker Department of Mechanical Engineering, The University of Texas at Austin

<sup>3</sup>Scripps Institution of Oceanography, University of California San Diego

<sup>4</sup>Department of Earth and Environmental Sciences, Ludwig-Maximilians-Universität München

## Abstract

Near-field tsunami early warning in the Cascadia Subduction Zone is limited by sparse offshore observations. We show that a hypothetical network of 175 seafloor pressure sensors can support real-time Bayesian inference of tsunamigenic seafloor motion and probabilistic tsunami forecasts for two fully-coupled Cascadia earthquake dynamic rupture–tsunami scenarios, a partial rupture and a margin-wide rupture. The complex oceanic acoustic, Rayleigh, and tsunami wavefields in both scenarios are similar during the first two minutes and then diverge. Using an acoustic–gravity inversion with offline precomputation and online assimilation of pressure data, tsunami forecasts are obtained in less than a second. We leverage a Bayesian inversion-based framework that splits the computations into an offline precomputation phase performed with large-scale computing facilities, and an online phase that computes forecasts from real-time data and can be executed on a laptop. Forecast errors remain low at 22.1% for the margin-wide rupture and 19.6% for the partial rupture.

**Keywords:** Bayesian inverse problems, tsunami early warning, Cascadia Subduction Zone, tsunamigenic megathrust earthquakes, fully-coupled dynamic rupture–tsunami simulations, real-time inference

## 1 Introduction

The most recent large megathrust earthquake on the Cascadia Subduction Zone (CSZ) occurred in 1700 (e.g., Atwater & Yamaguchi, 1991; Satake et al., 2003). However, the rupture extent of past and future Cascadia earthquakes remains uncertain, with (paleo-)geological, geophysical, and modeling studies supporting both partial- and margin-wide earthquake rupture scenarios (Walton et al., 2021; Melgar, 2021; Ramos et al., 2021; Small et al., 2025; Glehman et al., 2025; Goldfinger et al., 2025; DeSanto et al., 2025). Time-dependent recurrence modeling suggests a  $\sim 30\%$  chance of a magnitude 8+ earthquake in southern Cascadia in the next 50 years, and a  $\sim 15\%$  chance of a magnitude  $\sim 9$  Cascadia earthquake in the next 50 years (Wirth et al., 2025).

Because the rupture extent of future Cascadia megathrust earthquakes remains uncertain, numerical modeling is essential for identifying physically plausible scenarios consistent with past events such as the 1700 earthquake and tsunami. In Cascadia, coastal paleo-subsidence estimates provide key constraints on modeled slip heterogeneity and tsunami hazard (e.g., Atwater et al., 1995; Wang et al., 2013; Kemp et al., 2018; Salaree et al., 2021; Dunham et al., 2025). Dynamic rupture simulations provide a physics-based framework to test which rupture scenarios are mechanically viable under realistic initial conditions (e.g., Day, 1982; Olsen et al., 1997; Ramos et al., 2022).

---

Corresponding author: Stefan Henneking, [stefan@oden.utexas.edu](mailto:stefan@oden.utexas.edu)

Fully-coupled earthquake–tsunami models (e.g., Noguchi et al., 2016; Saito et al., 2019; Abrahams et al., 2023) link kinematic or dynamic rupture earthquake scenarios with acoustic wave propagation and tsunami gravity wave generation. This method was first introduced by Maeda and Furumura (2013) and subsequently used by Maeda et al. (2013) to study the 2011 Tohoku–Oki earthquake and tsunami. For Cascadia, fully-coupled dynamic rupture and tsunami simulations have previously been carried out using two-dimensional models (Lotto et al., 2019; Wilson & Ma, 2021). However, recent 3D dynamic rupture simulations constrained by Cascadia paleo-subsidence and kinematic geodetic coupling models (Ramos et al., 2021; Glehman et al., 2025; Biemiller et al., 2025) have not yet been extended to model the ensuing tsunami.

Tsunami early warning has traditionally relied on Deep-ocean Assessment and Reporting of Tsunamis buoys (DART, Gonzalez et al. (1998)), which remain a key component of operational real-time tsunami forecasting systems (e.g., Wei et al., 2008; Mungov et al., 2013; Tang et al., 2017). These systems are increasingly complemented by land-based seismic and geodetic observations (e.g., Kanamori & Rivera, 2008; Gusman & Tanioka, 2014; Crowell et al., 2016; Williamson et al., 2020), and combined seismo-geodetic approaches (e.g., Melgar & Bock, 2013; Golriz et al., 2023).

However, the sparsity of available sensors, particularly offshore, still limits the ability to constrain tsunami generation close to the source. Following the 2011 magnitude 9 Tohoku–Oki earthquake and tsunami, Japan deployed offshore sensor networks, including DONET and S-net. The latter consists of an array of 150 ocean bottom stations, equipped with pressure gauges and seismometers connected by about 5800 km of fiber-optic cable to improve earthquake and tsunami monitoring (e.g., Kanazawa, 2013; Tanioka & Gusman, 2018). These networks may enable rapid tsunami detection and forecasting from near-fault ocean-bottom pressure data (Aoi et al., 2020; Mizutani et al., 2020; Mulia & Satake, 2021). Similar offshore sensor networks for earthquake and tsunami early warning have been proposed for Cascadia (Saunders & Haase, 2018; Schmidt et al., 2019).

In this work, we demonstrate that if a network of comparable size to S-net existed in Cascadia, accurate real-time probabilistic tsunami forecasting would be feasible. We utilize a hypothetical network of 175 sensors, comparable in size to S-net, to drive a physics-based inversion framework. Prior work using near-field ocean-bottom pressure data for tsunami source characterization has typically employed low-dimensional parameterizations of earthquake source parameters, such as moment magnitude, hypocenter location, or simplified static slip distributions, matched either against precomputed scenario databases or against long-wave shallow-water forward models (Tsushima et al., 2009; Tanioka & Gusman, 2018; Mulia & Satake, 2021; Kubota et al., 2021). Unlike these approaches, our framework inverts directly for the full spatiotemporal seafloor velocity field, without assuming a source fault geometry or dislocation model, using a 3D coupled acoustic–gravity wave propagation model in the near-field, that captures the complex physics of the ocean–solid Earth interaction immediately following megathrust rupture.

This study extends the methodology and results previously presented in Henneking et al. (2025). Whereas that work demonstrated the computational scalability of the inverse solver for an idealized sensor configuration, this paper focuses on increased physical realism and application relevance. The key differences are as follows:

1. **More realistic source physics:** we transition from the solid Earth-only dynamic rupture scenarios (Glehman et al., 2025) used in Henneking et al. (2025) to fully-coupled dynamic rupture–tsunami models that include the interaction between the solid Earth and the ocean water layer. These sources provide a more physically consistent representation of the complex dynamics of the evolving seafloor motion during rupture and the energy transfer to the water column.
2. **Variable rupture scenarios:** whereas the previous work considered only margin-wide rupture events, we additionally introduce a partial rupture scenario. This is

important for assessing whether our system can distinguish between earthquakes of varying spatial extents.

3. **Realistic sensor network size:** the inversion in Henneking et al. (2025) used an array of 600 sensors spaced near-uniformly across the CSZ. Here, we instead perform the inversion using a much sparser network of 175 sensors, chosen to reflect a plausible deployment size comparable to S-net in Japan.

## 2 Methods

### 2.1 Cascadia fully-coupled dynamic rupture and tsunami simulations

We extend two physics-based Cascadia dynamic rupture scenarios to simulate fully-coupled earthquake–tsunami generation (Supporting Information, Table S1). We consider a partial rupture ( $M_W$  8.6) and a margin-wide rupture ( $M_W$  8.7) scenario, that is, Models 2 and 16 from Glehman et al. (2025). Each model combines the Slab2 Cascadia megathrust interface (Hayes et al., 2018) with realistic bathymetry and topography (GEBCO Bathymetric Compilation Group, 2020). Both use a linear-slip weakening friction law (e.g., Ida, 1972; Andrews, 1976), with a static friction coefficient of 0.6, a dynamic friction coefficient of 0.1, and a critical slip-weakening distance of 1.0 m, following Ramos et al. (2021). Both scenarios also assume the same hypocenter in northern Cascadia at 16 km depth, a pore fluid pressure ratio of 0.97 near lithostatic conditions, and a low rigidity structure (Sallarès & Ranero, 2019; Madden et al., 2022). The two models differ in their initial stress conditions. The partial rupture scenario has lower prestress in central Cascadia, creating a stress barrier that arrests rupture.

We use the open-source software SeisSol (Gabriel et al., 2025) for the fully-coupled earthquake dynamic rupture and tsunami simulations (Supporting Information, Text S1). To extend the Cascadia dynamic rupture scenarios to fully-coupled earthquake–tsunami simulations, we add a 3D acoustic layer representing the ocean atop the solid Earth. In this water layer, we set the shear modulus to zero and use a uniform density of  $1000 \text{ kg m}^{-3}$ , which governs the modeled acoustic and oceanic Rayleigh wave propagation. To model gravity tsunami waves, we apply a gravity-restoring boundary condition at the sea surface (Lotto & Dunham, 2015; Krenz et al., 2021). We define the sea surface height anomaly (ssa) as the deviation from the ocean surface at rest. For the Bayesian inversion framework explained in the next Section, the modeled seafloor velocities and resulting pressure time series are low-pass filtered and sampled at 1 Hz before assimilation.

### 2.2 Bayesian inversion framework

The approach used in this study combines fully-coupled earthquake–tsunami simulations for the Cascadia rupture scenarios (Section 2.1) with an acoustic–gravity model for the inference of tsunamigenic seafloor motion and tsunami forecasts from seafloor pressure observations. The fully-coupled simulations are used to generate physically-consistent synthetic rupture scenarios and synthetic ocean-bottom pressure data. The Bayesian inversion and tsunami forecasting are performed with the acoustic–gravity model. This choice enables us to resolve near-field coupled seismic–acoustic–gravity wave dynamics while retaining a computationally efficient forward and adjoint framework for real-time inference. Our Bayesian inversion assimilates the complete time history of synthetic seafloor pressure observations over the 420-second simulation window, capturing both the early high-frequency acoustic arrivals and the evolving longer-period pressure changes associated with the developing seafloor deformation and gravity wave generation.

The coupled acoustic–gravity wave equations model pressure perturbations and the forward propagation of tsunamis in a compressible ocean, thereby capturing the interaction between surface gravity waves and acoustic waves. The partial differential equations (PDEs) are derived by linearizing the mass and momentum conservation laws around a hydrostatic

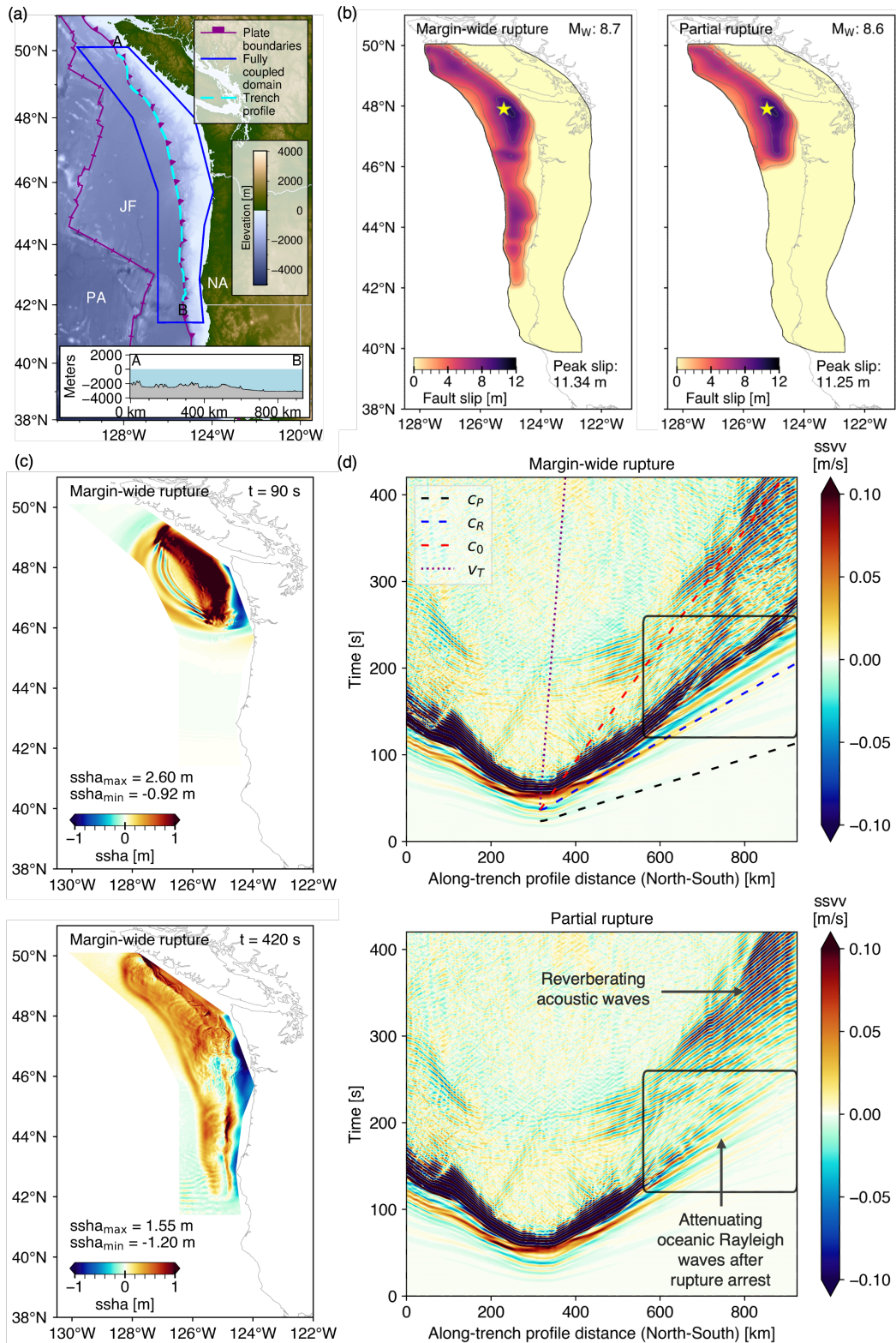


**Figure 1.** (a) Overview of the Pacific Northwest coast and major plate boundaries (Bird, 2003). The blue polygon outlines the domain for the 3D fully-coupled earthquake dynamic rupture and tsunami simulations performed with SeisSol (Gabriel et al., 2025). The dashed cyan line marks a densely spaced virtual receiver profile located at the sea surface, following the Juan de Fuca (JF) and North American (NA) plate boundary from 50°N to 42°N. (b) Earthquake slip distributions for the margin-wide and partial rupture fully-coupled simulations, closely matching the Solid Earth-only dynamic rupture scenarios of Glehman et al. (2025). (c) Sea surface height anomaly (ssha) for the margin-wide rupture scenario at 90 s, during tsunami generation, and at 420 s, at the end of the fully-coupled simulation. (d) Space-time evolution of sea surface vertical velocities (ssvv) along the trench profile for the margin-wide and partial rupture scenarios. Seismo-acoustic wave amplitudes dominate during the earthquake rupture and early tsunami generation phase. After rupture arrest, oceanic Rayleigh wave signals attenuate rapidly, whereas acoustic waves remain visible until the end of the modeled time window for both cases.

background state. The surface gravity wave enters through an adjusted kinematic free-surface boundary condition (Lotto & Dunham, 2015). The governing equations take the form of a coupled first-order system involving the fluid velocity  $\vec{u}(\vec{x}, t)$ , acoustic pressure  $p(\vec{x}, t)$ , and surface wave elevation  $\eta(\vec{x}, t)$ ,

$$\left\{ \begin{array}{ll} \rho \partial_t \vec{u} + \nabla p = 0, & \Omega \times (0, T), \\ K^{-1} \partial_t p + \nabla \cdot \vec{u} = 0, & \Omega \times (0, T), \\ p = \rho g \eta, & \partial\Omega_s \times (0, T), \\ \partial_t \eta = \vec{u} \cdot \vec{n}, & \partial\Omega_s \times (0, T), \\ \vec{u} \cdot \vec{n} = -m, & \partial\Omega_b \times (0, T), \\ \vec{u} \cdot \vec{n} = Z^{-1} p, & \partial\Omega_a \times (0, T), \end{array} \right. \quad (1)$$

subject to zero initial state conditions. In this formulation,  $\rho$  and  $K$  denote the water’s density and bulk modulus, respectively, defining the sound speed  $c = \sqrt{K/\rho}$  and acoustic impedance  $Z = \rho c$ . The variable  $g$  represents gravitational acceleration. The free surface  $\partial\Omega_s$ , the ocean floor  $\partial\Omega_b$ , and the artificial lateral absorbing boundaries  $\partial\Omega_a$  comprise the boundary of the compressible ocean domain  $\Omega$ . The vector  $\vec{n}$  denotes the outward-pointing unit normal, and the temporal domain is  $(0, T)$ . The forward model inputs are given by  $m(\vec{x}, t)$ , a spatiotemporal field that prescribes the (earthquake-induced) inward-pointing normal velocity of the seafloor.

The observables are the model predictions of ocean-bottom pressures  $d^{\text{obs}}$  obtained from seafloor sensors. The *quantities of interest* (QoI), denoted by  $q$ , represent model predictions of tsunami wave heights at target locations and times. Given seafloor pressure observations  $d^{\text{obs}}$ , the goal of the inversion framework is to (1) infer the uncertain (discretized) seafloor velocity parameters  $m$ , and (2) using the inferred parameters  $m$  as model inputs for the (discretized) acoustic–gravity equations, forecast the tsunami wave heights  $q$ .

The challenge with solving this inverse problem, in real time, is the computational cost of solving the acoustic–gravity model at high-enough resolution to accurately resolve the propagating ocean acoustic waves. While earthquake-induced seafloor motion contains a range of frequencies, the dominant acoustic wave frequencies are typically of the order of  $\sim 0.1$  Hz in the deep ocean (LeVeque et al., 2018; Levin & Nosov, 2015). The coupled acoustic–gravity model resolves a spectrum of frequencies from the long-period gravity wave regime up to 1 Hz (i.e., 1500 m wavelengths) of the propagating acoustic waves in the 3D compressible ocean domain, over the 1000 km long CSZ, which requires fine grids. For Cascadia, the discretized spatiotemporal seafloor velocities  $m$  consist of over one billion parameters. Moreover, the inference of this high-dimensional parameter vector from sparse and noisy pressure data is inherently ill-posed, as many different sets of parameters may be consistent with the limited observational data to within the noise tolerance.

To address this challenge, we adopt a Bayesian approach. Rather than seeking a single deterministic “best-fit” solution, Bayesian inference characterizes the probability that any given parameter field is consistent with both the observed data and any prior knowledge. The uncertain parameter field is treated as a random field, and the solution to the inverse problem is the posterior probability distribution (Kaipio & Somersalo, 2005; Stuart, 2010; Ghattas & Willcox, 2021). This probabilistic framework rigorously quantifies uncertainties in both the inverse solution and the resulting tsunami forecasts.

For the Cascadia inversion, the Bayesian solution characterizes the *posterior* probability density of the discretized seafloor velocities  $m$ , conditioned on the pressure observations  $d^{\text{obs}}$ . The subsequent predictive task propagates this inferred posterior through the forward model to obtain the *posterior predictive* of the tsunami wave heights  $q$ . In finite dimensions, Bayes’ rule states

$$\pi_{\text{post}}(m|d^{\text{obs}}) \propto \pi_{\text{like}}(d^{\text{obs}}|m) \pi_{\text{prior}}(m),$$

where  $\pi_{\text{post}}(\mathbf{m}|\mathbf{d}^{\text{obs}})$  denotes the posterior probability density of the parameters  $\mathbf{m}$  given observations  $\mathbf{d}^{\text{obs}}$ ;  $\pi_{\text{like}}(\mathbf{d}^{\text{obs}}|\mathbf{m})$  is the likelihood of observations, which measures data misfit; and  $\pi_{\text{prior}}(\mathbf{m})$  is the prior, which encapsulates any initial knowledge about the parameters.

Because the acoustic-gravity forward map and the forecast quantity-of-interest map are linear, and because we assume a Gaussian prior and an additive Gaussian noise model, which assumes the observed pressure signals are a sum of the true signals and Gaussian-distributed noise, the posteriors of the seafloor velocity parameters and the tsunami forecasts are also Gaussians, implying that the parameter inference becomes a linear inverse problem. Nonetheless, the high-dimensionality of the parameter space, the computational complexity of the discretized PDE model, and the wave propagation nature of the governing physics equations, imply that conventional methods are not capable of solving this linear inverse problem in real time (Henneking et al., 2025).

Instead, we employ a recently developed framework that exploits the linear time-invariant structure of the acoustic-gravity wave equations (Henneking et al., 2026). In this framework, the inverse solution is decomposed into several precomputation (offline) phases that are executed just once, before any earthquake occurs, and a real-time (online) phase of parameter inference and tsunami wave height forecasts that is executed when an earthquake occurs and data are acquired. The offline phases are computationally demanding and require performance-optimized implementations on large-scale computing systems (Tu et al., 2026). The framework’s most expensive step is precomputing one adjoint PDE solution of the acoustic-gravity model per sensor location and forecast location. The acoustic-gravity PDEs are discretized using high-order finite element methods and implemented via the MFEM library (Anderson et al., 2021). For Cascadia, each wave propagation solution takes approximately one hour on 512 GPUs.

Once these precomputations are completed, the remaining computations, both offline and online, do not require solving PDEs but instead exploit the time invariance property of the underlying physics model to perform fast and efficient FFT-based mappings from the parameter inputs to the observables (Venkat et al., 2025). In the online phase, given real-time data from seafloor sensors, the seafloor motion and tsunami wave heights are computed within fractions of a second. For a detailed discussion of this real-time Bayesian inference framework, we refer to Henneking et al. (2026) and references therein.

### 3 Results

#### 3.1 Fully-coupled margin-wide and partial dynamic rupture models

The addition of acoustic and gravity wave propagation within the added ocean layer does not alter the dynamic rupture extent and slip distribution in the margin-wide and partial rupture scenarios (Figure 1b) compared to Glehman et al. (2025)’s dynamic-rupture-only results: the margin-wide rupture scenario generates a moment magnitude of  $M_W$  8.7 and the partial rupture generates an  $M_W$  8.6 earthquake. The margin-wide scenario propagating southward from the hypocenter self-arrests at  $\sim 42^\circ\text{N}$ , whereas the partial rupture scenario self-arrests at  $\sim 46^\circ\text{N}$ , thus remaining constrained to off-shore Vancouver Island and Washington.

Both scenarios are characterized by a similar rupture behavior until the respective rupture fronts reach the central CSZ (Figure S1 in Supporting Information, Movies S1 & S2). For example, both models share comparable peak slip values of 11.34 m and 11.25 m, respectively (Supporting Information, Table S1), even though they are different in terms of rupture extent. However, fault slip in the margin-wide rupture scenario has lower slip values off-shore Oregon compared to slip north of  $\sim 46^\circ\text{N}$ .

The initial stages of tsunami generation in both fully-coupled simulations reflect the initial dynamic rupture source similarities (Figure 1c). Clear ssha deviations occur first after the margin-wide rupture breaks the central part of the CSZ. Peak ssha amplitudes for both

scenarios reach  $\sim 2.5$  m and  $\sim -1$  m after 60 s (Figure S2 in Supporting Information, Movies S3 & S4). After 120 s simulation time, we observe continued seismo-acoustic and gravity wave generation for the margin-wide, now solely southward rupture. During the 420 s of simulated time, tsunami amplitudes reach a maximum of 4.01 m and 2.93 m for the margin-wide and partial rupture scenario, respectively.

To analyze and compare the space-time evolution of sea surface vertical velocities (ssvv, Figure 1d), we place a line of receivers at the sea surface, following the location of the trench from  $50^\circ\text{N}$  to  $42^\circ\text{N}$  over a total distance of 923 km (Figure 1a). The modeled wavefield in the ocean is composed of multiple seismo-acoustic phases in addition to the long-period, dispersive tsunami gravity wave signal. The fastest, low-amplitude signals are associated with seismic P-waves, traveling at P-wave speed ( $c_P$ ) (Saito et al., 2019; Aniko Wirp et al., 2021). Oceanic Rayleigh waves follow, propagating slower than seismic body waves but faster than acoustic waves. As expected (e.g., Abrahams et al., 2023), these travel slightly slower compared to the solid Earth Rayleigh wave speed ( $c_R$ ), calculated using TauP and ObsPy (Crotwell et al., 1999; Beyreuther et al., 2010) using the 1D subsurface structure of the solid Earth from the dynamic rupture simulations. We observe a strong reduction in oceanic Rayleigh wave amplitudes in the partial rupture scenario once the rupture has arrested, whereas oceanic Rayleigh wave amplitudes remain large in the margin-wide rupture. In the southern part of the CSZ, strongly reverberating acoustic waves propagating with acoustic wave speeds ( $c_0=1500$  m/s) are present in the ocean acoustic medium for both rupture scenarios. The slowest signal is the vertical tsunami gravity wave, whose amplitudes remain small across the North–South trending profile. We measure an average tsunami speed as  $v_T = 158 \text{ m s}^{-1}$  for local bathymetry averaging at 2554 m along the trench profile.

### 3.2 Inference of seafloor motion and forecast of tsunami wave heights

The complex ground motions generated by the fully-coupled earthquake dynamic rupture and tsunami simulations of Section 3.1 are used to evaluate our real-time inversion methodology for Cascadia. Treating these ground motions as “ground truths” for the seafloor velocity parameter field, we use the forward acoustic–gravity solver to generate synthetic pressure observations at hypothetical sensor locations, which are sampled at 1 Hz, for each rupture scenario. We add 1% relative Gaussian noise to the pressure signals and compare two hypothetical sensor arrays consisting of  $N_d = 600$  versus  $N_d = 175$  pressure sensors. Given these synthetic observational data, we use the Bayesian inversion framework described in Section 2.2 to infer the earthquake-induced seafloor motion in the CSZ and forecast tsunami wave heights at  $N_q = 21$  designated locations.

The accuracy of (the mean of) the inferred parameters and tsunami wave height forecasts can be estimated by computing their relative errors (measured as l2 vector norms) against the ground truths. For the margin-wide rupture scenario, the relative errors of the inferred (spatiotemporal) seafloor normal displacement field are 29.6% (600 sensors) and 36.1% (175 sensors); and the relative errors of the tsunami wave height forecasts are 18.6% (600 sensors) and 22.1% (175 sensors). For the partial rupture scenario, the relative errors of the inferred seafloor displacements are 27.7% (600 sensors) and 31.7% (175 sensors); and the relative errors of the tsunami forecasts are 18.1% (600 sensors) and 19.6% (175 sensors).

The results of the parameter inference and tsunami wave height forecasts under uncertainty are shown in Figures 2 and 3 for both the margin-wide and the partial rupture scenario. The “ground truths” generated by the fully-coupled dynamic rupture–tsunami simulations and (the means of) the inverse solutions in Figure 2 are depicted in terms of the final seafloor normal displacement,  $\int_0^T m(\vec{x}, t) dt$ , at  $T = 420$  s, which is visually simpler to interpret than snapshots of the true and inferred spatiotemporal parameter fields (seafloor velocities). Similarly, the associated uncertainties of the Bayesian inverse solutions are shown as pointwise standard deviations of the final seafloor normal displacements in Figure 2. The tsunami wave height forecasts in Figure 3 are in each case (top row: margin-wide rupture;

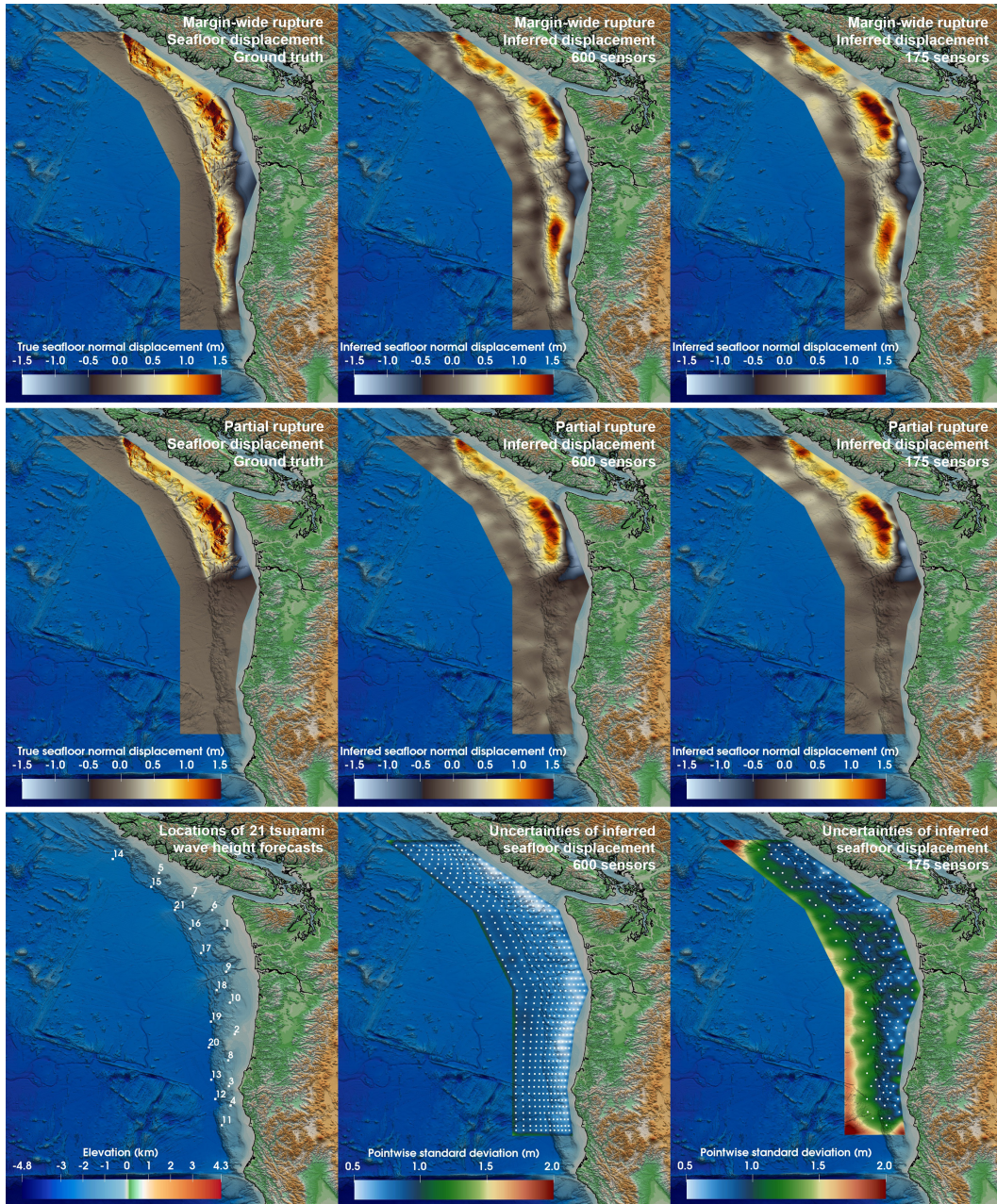


**Figure 2.** Snapshots of the true (left column) and inferred (middle and right columns) seafloor normal displacements at the final time ( $t = 420$  seconds) for a margin-wide rupture (top row) and partial rupture (middle row) scenario, and their associated uncertainties given as pointwise standard deviations (bottom row). Results in the middle and right columns respectively correspond to inversion using synthetic data from 600 and 175 hypothesized ocean bottom pressure sensors, with the sensor locations marked in the corresponding uncertainty plots of the bottom row. The bottom left plot depicts ocean bathymetry with the 21 tsunami wave height forecasting locations.

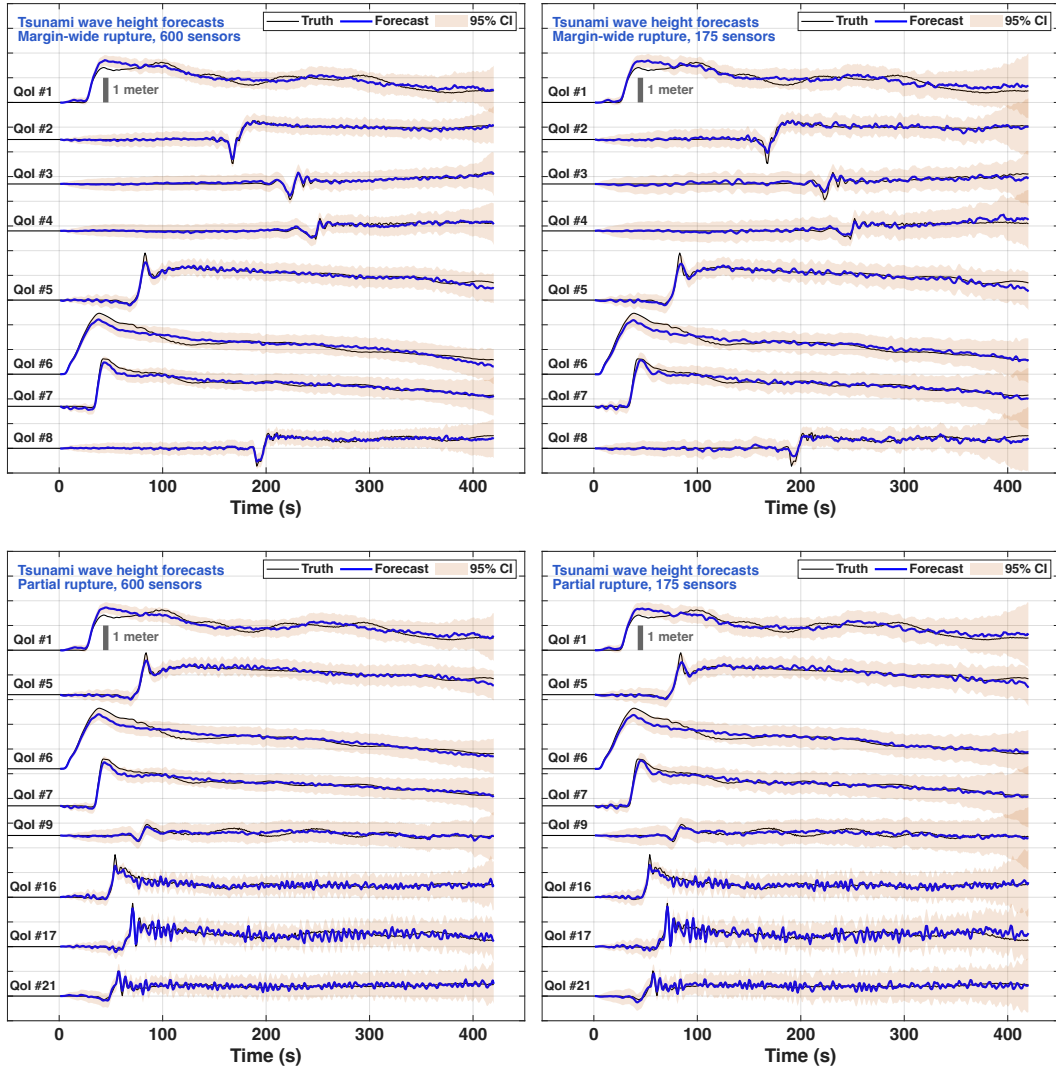


**Figure 3.** Tsunami wave height forecasts and their uncertainties (depicted as 95% credible intervals) at a subset of the 21 target locations (labeled as QoI #1–#21, with locations as shown in the bottom left plot of Figure 2), obtained with 600 sensors (left column) and 175 sensors (right column), for the margin-wide rupture (top row) and partial rupture scenarios (bottom row). The relative errors of the tsunami forecasts are 18.6% (600 sensors) and 22.1% (175 sensors) for the margin-wide rupture, showing only a modest degradation of the forecast quality with the sparser sensor network. Similar tsunami forecast errors of 18.1% (600 sensors) and 19.6% (175 sensors) are obtained for the partial rupture scenario.

bottom row: partial rupture) shown for a subset of the 21 target forecasting locations depicted in the bottom left plot of Figure 2. The forecasts are compared against the synthetic truths generated by the acoustic-gravity model using the “ground truth” seafloor velocity fields from the dynamic rupture models as an input. The time-dependent uncertainties associated with each forecast are illustrated as 95% credible intervals (CIs) around the mean of each forecast.

The inverse solutions show that a sparse network of 175 offshore pressure sensors supports accurate real-time tsunami forecasts in the CSZ. The forecasts with 175 sensors are nearly as accurate as the ones obtained with 600 sensors, in both the margin-wide rupture and the partial rupture scenario. The inferred seafloor displacements have larger errors than the tsunami forecasts, and Figure 2 shows that these errors are primarily due to the inability of inferring the fine spatial scales of the seafloor uplift. Thus, while sparse offshore pressure observations in the near field are not sufficient to recover all components of the displacement field accurately, the *tsunamigenic* components of the seafloor motion are recovered with good accuracy. For both the seafloor displacements and the tsunami forecasts, the inverse solution with 175 sensors clearly distinguishes the margin-wide rupture from the partial rupture scenario.

## 4 Discussion

### 4.1 Implications for near-field tsunami forecasting

The fully-coupled earthquake dynamic rupture and tsunami models illustrate that near-field ocean-bottom pressure signals contain not only the emerging tsunami signals but also faster seismo-acoustic phases, including oceanic Rayleigh waves and acoustic waves that may accompany submarine earthquakes (e.g., Nakamura et al., 2012; Kozdon & Dunham, 2014; Abdolali et al., 2015). In the margin-wide and partial rupture scenario considered here, all of these phases are excited similarly during the first two minutes of earthquake rupture propagation, which limits very rapid discrimination between partial and margin-wide rupture in our framework. After rupture arrest in the partial scenario, however, seismo-acoustic signals divert, which suggests that the early seismo-acoustic wavefield may provide information on rupture extent before the tsunami signal itself becomes diagnostic, which could be relevant for operational near-field tsunami warning (e.g., Melgar et al., 2016). Future work could extend our analysis to other rupture scenarios, including events nucleating in southern Cascadia or exhibiting different along-strike (prestress/friction) segmentation (Ramos et al., 2021; Wirth et al., 2025; Small et al., 2025), and alternative megathrust geometries and 3D structural models (Carbotte et al., 2024; Dunham et al., 2025; Kwong et al., 2025). Additionally, simulations with coseismic splay faulting or off-fault plastic deformation could be investigated (Wendt et al., 2009; Ulrich et al., 2022; Ma, 2023; Ma & Du, 2025; Biemiller et al., 2025), as well as other subduction margins (Wirp et al., 2025; Wong et al., 2026).

Among these possible extensions, uncertainty in the prescribed fault geometry is likely especially important because both coseismic seafloor deformation and tsunami generation depend on the assumed megathrust interface (Lotto et al., 2019; Kwong et al., 2025; Dunham et al., 2025). The dynamic rupture models considered here use the Slab2 Cascadia megathrust geometry (Hayes et al., 2018), whereas recent regional-scale seismic imaging of the Cascadia margin (Carbotte et al., 2024) suggests a shallower subduction interface. Likewise, although a Nankai-style megasplay fault system is not likely to exist in Cascadia (Lucas et al., 2023), smaller regional splays may contribute to source complexity and tsunami generation (e.g., Wendt et al., 2009; van Zelst et al., 2022; Biemiller et al., 2025).

## 4.2 Implications for real-time tsunami forecasting

Given real-time near-field pressure transients, our Bayesian inversion-based framework infers seafloor motion and produces probabilistic tsunami wave height forecasts at selected offshore target locations within fractions of a second (Henneking et al., 2025). If only tsunami forecasts are required, without reconstruction of the full seafloor displacement field, the real-time inference can be performed with minimal computing infrastructure, for example, on a laptop (Henneking et al., 2026). Here, we demonstrate the framework for 21 forecast locations. Noting that even a limited number of tsunami wave height forecasts is informative for early warning purposes (Liu et al., 2021), this number could readily be increased to several hundred forecast locations while retaining real-time forecast capability with modest compute resources.

To evaluate the acoustic-gravity Bayesian inversion framework, we use complex, earthquake-induced seafloor velocity fields generated by fully-coupled dynamic rupture simulations with elastic-acoustic-gravity wave propagation. One could, in principle, solve instead an inverse problem for the fault slip using the coupled Earth-ocean system. The 3-field elastic-acoustic-gravity system remains linear time-invariant, thus, our current inversion framework might still be executable in real time. However, in addition to much greater offline cost due to solving the computationally more demanding 3-field system (Supplementary Information, Text S1), there are several reasons to invert for seafloor motion using the acoustic-gravity model over using the fully-coupled system in the inversion.

Inverting for fault slip rather than seafloor motion would introduce additional uncertainty from seismic velocity structure and fault geometry into the inverse problem (e.g., Beresnev, 2003; Duputel et al., 2014; Ragon et al., 2018). By contrast, uncertainties in ocean acoustic wave speed due to seawater temperature, salinity, bulk modulus, and density are comparatively small (e.g., Mackenzie, 1981; Dushaw et al., 1993). In addition, excluding the elastic solid in the inversion avoids assuming that seafloor uplift arises only from coseismic elastic deformation, and in principle allows extension to other tsunami sources, such as mass slumping, landslides, (volcanic) explosions, or inelastic coseismic deformation (e.g., Duffy, 1992; Grilli & Watts, 2005; Løvholt et al., 2015; Schulten et al., 2019; Schindelé et al., 2024; Svennevig et al., 2024; Du & Ma, 2025). Because our goal is to infer seafloor motion in real time and use it to forecast tsunami propagation, it is not necessary to include the elastic solid in the inverse problem: although seafloor motion in our models originates from the coupled solid Earth-ocean system, the mapping from seafloor motion to the induced pressure transients and gravity-wave excitation is captured by the acoustic-gravity model.

Our results indicate that relatively sparse near-field pressure observations are sufficient to infer the smooth, tsunami-relevant components of seafloor motion and that these components account well for the surface gravity wave generation. This is reflected in the substantially smaller relative errors of the tsunami wave height forecasts (18.1%–22.1%) compared to those of the inferred seafloor displacements (27.7%–36.1%). Furthermore, the inference of these smooth components deteriorates only slowly as the number of sensors is reduced from 600 to 175, with relative errors in the inferred seafloor displacement field increasing from 29.6% to 36.1% for the margin-wide rupture and from 27.7% to 31.7% for the partial rupture scenarios. The corresponding relative errors of the tsunami wave height forecasts increase even more slowly, from 18.6% to 22.1% and from 18.1% to 19.6%, respectively.

The modest degradation in tsunami forecast accuracy with decreasing sensors from 600 to 175 indicates that the forecasts are relatively robust to sensor sparsification. This may suggest that further reducing the number of sensors would still achieve reasonably accurate forecasts across the CSZ, although the inferred seafloor motion and associated uncertainties deteriorate more strongly, as quantified by the Bayesian framework through the relative increase of the credible intervals from the left column to the right column plots of Figure 3.

We note that the 175-sensor network considered here was placed ad-hoc, without optimization of sensor locations. Rather than prescribing sensor locations a priori, future work can address the design challenge of optimal sensor placement, given a fixed budget. In the Bayesian framework, future work can pose such an *optimal experimental design* (OED) problem (e.g., Atkinson et al., 2007; Pukelsheim, 2006)) as an optimization problem that maximizes the expected information gain from the sensor observations, resulting in the smallest uncertainties of the inferred solution (e.g., Ghattas & Willcox, 2021; Alexanderian et al., 2016). This information gain could also be tailored to be goal-oriented (e.g., Attia et al., 2018; Wu et al., 2023), prioritizing sensor locations that most reduce tsunami forecast uncertainty in location and time most relevant for tsunami early warning and hazard or risk mitigation in Cascadia.

## 5 Conclusions

This study applies a physics-based Bayesian inversion framework for real-time, data-driven tsunami forecasting for Cascadia with dynamic adaptivity to complex source behavior. Following an earthquake, the framework assimilates near-field ocean-bottom pressure observations to infer the earthquake-induced spatiotemporal seafloor motion, and uses this inverse solution to forecast tsunami propagation. The inversion and tsunami forecasting employs an acoustic-gravity model that captures coupled ocean acoustic and tsunami wave propagation. Both the inferred seafloor motion and the tsunami forecasts are accompanied by quantified uncertainty estimates. Because the most expensive computations of the inversion are shifted to an offline precomputation stage performed before any earthquake occurs, real-time inference can be carried out in less than a second once observations are available.

Using two fully-coupled Cascadia dynamic rupture–tsunami scenarios, we show that early tsunami-source discrimination is nontrivial. The initial near-field ocean-bottom pressure signals are similar for partial and margin-wide ruptures. However, on the timescale of minutes after earthquake rupture onset, the scenarios become distinguishable as the partial rupture arrests earlier and its oceanic Rayleigh waves attenuate more rapidly. On these timescales, the inversion framework is able to clearly differentiate between these two rupture scenarios.

For a hypothetical offshore pressure network of 175 sensors, comparable in scale to Japan’s S-net, the relative tsunami forecast errors are 22.1% for the margin-wide rupture and 19.6% for the partial rupture, which represents only a modest degradation relative to a denser 600-sensor configuration. Together, these results are an important step toward physics-consistent, real-time probabilistic tsunami forecasting in the Cascadia Subduction Zone and motivate future off-shore ocean-bottom sensor deployments.

## Conflict of Interest declaration

The authors declare there are no conflicts of interest for this manuscript.

## Acknowledgments

Stefan Henneking, Fabian Kutschera, and Sreeram Venkat contributed equally to this work.

This research was supported by DARPA COMPASS HR0011-25-3-0242, DOD MURI grant FA9550-24-1-0327 and DOE ASCR grant DE-SC0023171. FK and AAG acknowledge support from the National Science Foundation (NSF grant numbers EAR-2225286, EAR-2121568, OAC-2139536, OAC-2311208, RISE-2531036), and the National Aeronautics and Space Administration (NASA 80NSSC20K0495). Horizon Europe (Geo-INQUIRE, grant number 101058518 and ChEESE-2P, grant number 101093038).

This research used resources from the National Energy Research Scientific Computing Center (NERSC; ALCC-ERCAP0030671, ScienceAtScale DDR-ERCAP0034808 and NESAP DDR-ERCAP0038013). The authors acknowledge the Texas Advanced Computing Center (TACC) at The University of Texas at Austin for providing computational resources that have contributed to the research results reported within this paper. Additional computing resources were provided by the Institute of Geophysics of LMU Munich (Oeser et al., 2006).

## References

- Abdolali, A., Cecioni, C., Bellotti, G., & Kirby, J. T. (2015). Hydro-acoustic and tsunami waves generated by the 2012 Haida Gwaii earthquake: Modeling and in situ measurements. *Journal of Geophysical Research: Oceans*, *120*(2), 958–971. doi: 10.1002/2014JC010385
- Abrahams, L. S., Krenz, L., Dunham, E. M., Gabriel, A.-A., & Saito, T. (2023). Comparison of methods for coupled earthquake and tsunami modelling. *Geophysical Journal International*, *234*(1), 404–426. doi: 10.1093/gji/ggad053
- Alexanderian, A., Gloor, P. J., & Ghattas, O. (2016). On Bayesian A-and D-optimal experimental designs in infinite dimensions. *Bayesian Analysis*, *11*(3), 671–695. doi: 10.1214/15-BA969
- Anderson, R., Andrej, J., Barker, A., Bramwell, J., Camier, J.-S., Cerveny, J., ... Zampini, S. (2021). MFEM: A modular finite element methods library. *Computers & Mathematics with Applications*, *81*, 42–74. doi: 10.1016/j.camwa.2020.06.009
- Andrews, D. J. (1976). Rupture velocity of plane strain shear cracks. *Journal of Geophysical Research*, *81*(32), 5679–5687. doi: 10.1029/JB081I032P05679
- Aniko Wirp, S., Gabriel, A.-A., Schmeller, M., H. Madden, E., van Zelst, I., Krenz, L., ... Rannabauer, L. (2021). 3D linked subduction, dynamic rupture, tsunami, and inundation modeling: Dynamic effects of supershear and tsunami earthquakes, hypocenter location, and shallow fault slip. *Frontiers in Earth Science*, *9*, 626844.
- Aoi, S., Asano, Y., Kunugi, T., Kimura, T., Uehira, K., Takahashi, N., ... Fujiwara, H. (2020). MOWLAS: NIED observation network for earthquake, tsunami and volcano. *Earth, Planets and Space*, *72*(1), 126. doi: 10.1186/s40623-020-01250-x
- Atkinson, A., Donev, A., & Tobias, R. (2007). *Optimum Experimental Designs, with SAS* (Vol. 34). OUP Oxford. doi: 10.1093/oso/9780199296590.001.0001
- Attia, A., Alexanderian, A., & Saibaba, A. K. (2018). Goal-oriented optimal design of experiments for large-scale Bayesian linear inverse problems. *Inverse Problems*, *34*(9), 095009. doi: 10.1088/1361-6420/aad210
- Atwater, B. F., Nelson, A. R., Clague, J. J., Carver, G. A., Yamaguchi, D. K., Bobrowsky, P. T., ... Reinhart, M. A. (1995). Summary of coastal geologic evidence for past great earthquakes at the Cascadia Subduction Zone. *Earthquake Spectra*, *11*(1), 1–18. doi: 10.1193/1.1585800
- Atwater, B. F., & Yamaguchi, D. K. (1991). Sudden, probably coseismic submergence of Holocene trees and grass in coastal Washington State. *Geology*, *19*(7), 706–709. doi: 10.1130/0091-7613(1991)019<0706:SPCSOH>2.3.CO;2
- Beresnev, I. A. (2003). Uncertainties in finite-fault slip inversions: To what extent to believe? (a critical review). *Bulletin of the Seismological Society of America*, *93*(6), 2445–2458. doi: 10.1785/0120020225
- Beyreuther, M., Barsch, R., Krischer, L., Megies, T., Behr, Y., & Wassermann, J. (2010). ObsPy: A Python toolbox for seismology. *Seismological Research Letters*, *81*(3), 530–533. doi: 10.1785/gssrl.81.3.530
- Biemiller, J., Gabriel, A.-A., Staisch, L., Ulrich, T., Dunham, A., Wirth, E., ... Ledeczi, A. (2025). Structural controls on splay fault rupture dynamics during Cascadia megathrust earthquakes. *AGU Advances*, *6*(6), e2025AV001812. doi: 10.1029/2025AV001812
- Bird, P. (2003). An updated digital model of plate boundaries. *Geochemistry, Geophysics, Geosystems*, *4*(3), 2001GC000252. doi: 10.1029/2001GC000252
- Carbotte, S. M., Boston, B., Han, S., Shuck, B., Beeson, J., Canales, J. P., ... Gahlawat,

- R. (2024). Subducting plate structure and megathrust morphology from deep seismic imaging linked to earthquake rupture segmentation at Cascadia. *Science Advances*, *10*(23), eadl3198. doi: 10.1126/sciadv.adl3198
- Crotwell, H. P., Owens, T. J., & Ritsema, J. (1999). The TauP toolkit: Flexible seismic travel-time and ray-path utilities. *Seismological Research Letters*, *70*(2), 154–160. doi: 10.1785/gssrl.70.2.154
- Crowell, B. W., Schmidt, D. A., Bodin, P., Vidale, J. E., Gomberg, J., Renate Hartog, J., ... Jamison, D. G. (2016). Demonstration of the Cascadia G-FAST geodetic earthquake early warning system for the Nisqually, Washington, Earthquake. *Seismological Research Letters*, *87*(4), 930–943. doi: 10.1785/0220150255
- Day, S. M. (1982). Three-dimensional simulation of spontaneous rupture: The effect of nonuniform prestress. *Bulletin of the Seismological Society of America*, *72*(6A), 1881–1902. doi: 10.1785/BSSA07206A1881
- DeSanto, J. B., Schmidt, D. A., Zumbege, M., Sasagawa, G., & Chadwell, C. D. (2025). Near full locking on the shallow megathrust of the central Cascadia Subduction Zone revealed by GNSS-Acoustic. *Earth and Planetary Science Letters*, *665*, 119463. doi: 10.1016/j.epsl.2025.119463
- Du, Y., & Ma, S. (2025). Wedge inelasticity and fully coupled models of dynamic rupture, ocean acoustic waves, and tsunami in the Japan Trench: The 1896 Sanriku earthquake. *Journal of Geophysical Research: Solid Earth*, *130*(10), e2025JB032410. doi: 10.1029/2025JB032410
- Duffy, D. G. (1992). On the generation of oceanic surface waves by underwater volcanic explosions. *Journal of volcanology and geothermal research*, *50*(3), 323–344.
- Dumbser, M., & Käser, M. (2006). An arbitrary high-order discontinuous Galerkin method for elastic waves on unstructured meshes - II. The three-dimensional isotropic case. *Geophysical Journal International*, *167*(1), 319–336. doi: 10.1111/j.1365-246X.2006.03120.x
- Dunham, A. M., Kim, J., Wirth, E., Schmidt, D., LeVeque, R. J., Wei, Y., ... Pollitz, F. (2025). The impact of 3D structure on coseismic coastal land-level change and tsunami generation in the Cascadia Subduction Zone. *Geophysical Research Letters*, *52*(24), e2025GL117783. doi: 10.1029/2025GL117783
- Duputel, Z., Agram, P. S., Simons, M., Minson, S. E., & Beck, J. L. (2014). Accounting for prediction uncertainty when inferring subsurface fault slip. *Geophysical Journal International*, *197*(1), 464–482. doi: 10.1093/gji/ggt517
- Dushaw, B. D., Worcester, P. F., Cornuelle, B. D., & Howe, B. M. (1993). On equations for the speed of sound in seawater. *The Journal of the Acoustical Society of America*, *93*(1), 255–275. doi: 10.1121/1.405660
- Gabriel, A.-A., Kurapati, V., Niu, Z., Schliwa, N., Schneller, D., Ulrich, T., ... Bader, M. (2025). *SeisSol*. Zenodo. doi: 10.5281/zenodo.4672483
- GEBCO Bathymetric Compilation Group. (2020). *GEBCO 2020 Grid*. doi: 10.5285/a29c5465-b138-234d-e053-6c86abc040b9
- Ghattas, O., & Willcox, K. (2021). Learning physics-based models from data: Perspectives from inverse problems and model reduction. *Acta Numerica*, *30*, 445–554. doi: 10.1017/S0962492921000064
- Glehman, J., Gabriel, A., Ulrich, T., Ramos, M., Huang, Y., & Lindsey, E. (2025). Partial ruptures governed by the complex interplay between geodetic slip deficit, rigidity, and pore fluid pressure in 3D Cascadia dynamic rupture simulations. *Seismica*, *2*(4). doi: 10.26443/seismica.v2i4.1427
- Goldfinger, C., Beeson, J., Black, B., Vizcaino, A., Nelson, C., Morey, A., ... Walczak, M. (2025). Unravelling the dance of earthquakes: Evidence of partial synchronization of the northern San Andreas fault and Cascadia megathrust. *Geosphere*. doi: 10.1130/GES02857.1
- Golriz, D., Hirshorn, B., Bock, Y., Weinstein, S., & Weiss, J. R. (2023). Real-time seismo-geodetic earthquake magnitude estimates for local tsunami warnings. *Journal of Geophysical Research: Solid Earth*, *128*(1), e2022JB025555. doi: 10.1029/2022JB025555

- Gonzalez, F. I., Milburn, H. M., Bernard, E. N., & Newman, J. C. (1998). Deep-ocean assessment and reporting of tsunamis (DART): Brief overview and status report. In *Proceedings of the international workshop on tsunami disaster mitigation*. Tokyo, Japan.
- Grilli, S. T., & Watts, P. (2005). Tsunami generation by submarine mass failure. I: Modeling, experimental validation, and sensitivity analyses. *Journal of waterway, port, coastal, and ocean engineering*, *131*(6), 283–297.
- Gusman, A. R., & Tanioka, Y. (2014). W phase inversion and tsunami inundation modeling for tsunami early warning: Case study for the 2011 Tohoku event. *Pure and Applied Geophysics*, *171*(7), 1409–1422. doi: 10.1007/s00024-013-0680-z
- Harris, R. A., Aagaard, B., Barall, M., Ma, S., Roten, D., Olsen, K., . . . Dalguer, L. (2018). A suite of exercises for verifying dynamic earthquake rupture codes. *Seismological Research Letters*, *89*(3), 1146–1162. doi: 10.1785/0220170222
- Hayes, G. P., Moore, G. L., Portner, D. E., Hearne, M., Flamme, H., Furtney, M., & Smoczyk, G. M. (2018). Slab2, a comprehensive subduction zone geometry model. *Science*, *362*(6410), 58–61. doi: 10.1126/science.aat4723
- Henneking, S., Venkat, S., Dobrev, V., Camier, J., Kolev, T., Fernando, M., . . . Ghattas, O. (2025). Real-time Bayesian inference at extreme scale: A digital twin for tsunami early warning applied to the Cascadia Subduction Zone. In *Proceedings of the international conference for high performance computing, networking, storage and analysis* (p. 60–71). New York, NY, USA: Association for Computing Machinery. doi: 10.1145/3712285.3771787
- Henneking, S., Venkat, S., & Ghattas, O. (2026). Goal-oriented real-time Bayesian inference for linear autonomous dynamical systems with application to digital twins for tsunami early warning. *Journal of Computational Physics*, *552*, 114682. doi: 10.1016/j.jcp.2026.114682
- Ida, Y. (1972). Cohesive force across the tip of a longitudinal-shear crack and Griffith’s specific surface energy. *Journal of Geophysical Research*, *77*(20), 3796–3805. doi: 10.1029/JB077I020P03796
- Kaipio, J., & Somersalo, E. (2005). *Statistical and Computational Inverse Problems* (Vol. 160). New York, NY: Springer-Verlag. doi: 10.1007/b138659
- Kanamori, H., & Rivera, L. (2008). Source inversion of W phase: Speeding up seismic tsunami warning. *Geophysical Journal International*, *175*(1), 222–238. doi: 10.1111/j.1365-246X.2008.03887.x
- Kanazawa, T. (2013). Japan Trench earthquake and tsunami monitoring network of cable-linked 150 ocean bottom observatories and its impact to earth disaster science. In *2013 IEEE International Underwater Technology Symposium (UT)* (pp. 1–5). doi: 10.1109/UT.2013.6519911
- Käser, M., & Dumbser, M. (2006). An arbitrary high-order discontinuous Galerkin method for elastic waves on unstructured meshes - I. The two-dimensional isotropic case with external source terms. *Geophysical Journal International*, *166*(2), 855–877. doi: 10.1111/j.1365-246X.2006.03051.x
- Kemp, A. C., Cahill, N., Engelhart, S. E., Hawkes, A. D., & Wang, K. (2018). Revising estimates of spatially variable subsidence during the A.D. 1700 Cascadia earthquake using a Bayesian foraminiferal transfer function. *Bulletin of the Seismological Society of America*, *108*(2), 654–673. doi: 10.1785/0120170269
- Kozdon, J. E., & Dunham, E. M. (2014). Constraining shallow slip and tsunami excitation in megathrust ruptures using seismic and ocean acoustic waves recorded on ocean-bottom sensor networks. *Earth and Planetary Science Letters*, *396*, 56–65. doi: 10.1016/j.epsl.2014.04.001
- Krenz, L., Uphoff, C., Ulrich, T., Gabriel, A.-A., Abrahams, L. S., Dunham, E. M., & Bader, M. (2021). 3D acoustic-elastic coupling with gravity: The dynamics of the 2018 Palu, Sulawesi earthquake and tsunami. In *Proceedings of the international conference for high performance computing, networking, storage and analysis* (pp. 1–14). doi: 10.1145/3458817.3476173

- Kubota, T., Saito, T., Tsushima, H., Hino, R., Ohta, Y., Suzuki, S., & Inazu, D. (2021). Extracting Near-Field Seismograms From Ocean-Bottom Pressure Gauge Inside the Focal Area: Application to the 2011 Mw 9.1 Tohoku-Oki Earthquake. *Geophysical Research Letters*, *48*(7), e2020GL091664. doi: 10.1029/2020GL091664
- Kutschera, F., Gabriel, A.-A., Dunham, E. M., Harris, R., Barall, M., Bachelot, L., ... Zhang, W. (2025). The CRESCENT/SCEC/USGS tsunami benchmarks: 3D fully coupled earthquake dynamic rupture and tsunami simulations with varying bathymetric complexity. In *Abstract (T43E-0182) presented at AGU25, 15-19 Dec.* AGU Annual Meeting 2025.
- Kwong, K., Crowell, B., Williamson, A., Melgar, D., & Wei, Y. (2025). Performance of slab geometry constraints on rapid geodetic slip models, tsunami amplitude, and inundation estimates in Cascadia. *Seismica*, *2*(4). doi: 10.26443/seismica.v2i4.1406
- LeVeque, R. J., Bodin, P., Cram, G., Crowell, B. W., González, F. I., Harrington, M., ... Wilcock, W. S. D. (2018). Developing a warning system for inbound tsunamis from the Cascadia subduction zone. In *Oceans 2018 mts/ieee charleston* (pp. 1–10). doi: 10.1109/OCEANS.2018.8604709
- Levin, B., & Nosov, M. (2015). *Physics of Tsunamis*. Springer Cham. doi: 10.1007/978-3-319-24037-4
- Liu, C. M., Rim, D., Baraldi, R., & LeVeque, R. J. (2021). Comparison of machine learning approaches for tsunami forecasting from sparse observations. *Pure and Applied Geophysics*, *178*(12), 5129–5153. doi: 10.1007/s00024-021-02841-9
- Lotto, G. C., & Dunham, E. M. (2015). High-order finite difference modeling of tsunami generation in a compressible ocean from offshore earthquakes. *Computational Geosciences*, *19*(2), 327–340. doi: 10.1007/s10596-015-9472-0
- Lotto, G. C., Jeppson, T. N., & Dunham, E. M. (2019). Fully coupled simulations of megathrust earthquakes and tsunamis in the Japan Trench, Nankai Trough, and Cascadia Subduction Zone. *Pure and Applied Geophysics*, *176*(9), 4009–4041. doi: 10.1007/S00024-018-1990-Y
- Lucas, M. C., Ledeczi, A. M., Tobin, H. J., Carbotte, S. M., Watt, J. T., Han, S., ... Jiang, D. (2023). No evidence for an active margin-spanning megasplay fault at the Cascadia Subduction Zone. *Seismica*, *2*(4). doi: 10.26443/seismica.v2i4.1477
- Løvholt, F., Pedersen, G., Harbitz, C. B., Glimsdal, S., & Kim, J. (2015). On the characteristics of landslide tsunamis. *Philosophical Transactions of the Royal Society A: Mathematical, Physical and Engineering Sciences*, *373*(2053), 20140376. doi: 10.1098/rsta.2014.0376
- Ma, S. (2023). Wedge plasticity and a minimalist dynamic rupture model for the 2011 MW 9.1 Tohoku-Oki earthquake and tsunami. *Tectonophysics*, *869*, 230146. doi: 10.1016/j.tecto.2023.230146
- Ma, S., & Du, Y. (2025). Wedge inelasticity and fully coupled models of dynamic rupture, ocean acoustic waves, and tsunami in the Japan Trench: The 2011 Tohoku-Oki earthquake. *Tectonophysics*, *910*, 230831. doi: 10.1016/j.tecto.2025.230831
- Mackenzie, K. V. (1981). Nine-term equation for sound speed in the oceans. *The Journal of the Acoustical Society of America*, *70*(3), 807–812. doi: 10.1121/1.386920
- Madden, E. H., Ulrich, T., & Gabriel, A.-A. (2022). The state of pore fluid pressure and 3-D megathrust earthquake dynamics. *Journal of Geophysical Research: Solid Earth*, *127*(4), e2021JB023382. doi: 10.1029/2021JB023382
- Maeda, T., & Furumura, T. (2013). FDM simulation of seismic waves, ocean acoustic waves, and tsunamis based on tsunami-coupled equations of motion. *Pure and Applied Geophysics*, *170*(1), 109–127. doi: 10.1007/s00024-011-0430-z
- Maeda, T., Furumura, T., Noguchi, S., Takemura, S., Sakai, S., Shinohara, M., ... Lee, S. J. (2013). Seismic- and tsunami-wave propagation of the 2011 off the Pacific Coast of Tohoku earthquake as inferred from the tsunami-coupled finite-difference simulation. *Bulletin of the Seismological Society of America*, *103*(2B), 1456–1472. doi: 10.1785/0120120118
- Melgar, D. (2021). Was the January 26th, 1700 Cascadia earthquake part of a rupture

- sequence? *Journal of Geophysical Research: Solid Earth*, 126(10), e2021JB021822. doi: 10.1029/2021JB021822
- Melgar, D., Allen, R. M., Riquelme, S., Geng, J., Bravo, F., Baez, J. C., . . . Smalley Jr., R. (2016). Local tsunami warnings: Perspectives from recent large events. *Geophysical Research Letters*, 43(3), 1109–1117. doi: 10.1002/2015GL067100
- Melgar, D., & Bock, Y. (2013). Near-field tsunami models with rapid earthquake source inversions from land- and ocean-based observations: The potential for forecast and warning. *Journal of Geophysical Research: Solid Earth*, 118(11), 5939–5955. doi: 10.1002/2013JB010506
- Mizutani, A., Yomogida, K., & Tanioka, Y. (2020). Early tsunami detection with near-fault ocean-bottom pressure gauge records based on the comparison with seismic data. *Journal of Geophysical Research: Oceans*, 125(9), e2020JC016275. doi: 10.1029/2020JC016275
- Mulia, I. E., & Satake, K. (2021). Synthetic analysis of the efficacy of the S-net system in tsunami forecasting. *Earth, Planets and Space*, 73(1), 36. doi: 10.1186/s40623-021-01368-6
- Mungov, G., Eblé, M., & Bouchard, R. (2013). DART® tsunameter retrospective and real-time data: A reflection on 10 years of processing in support of tsunami research and operations. *Pure and Applied Geophysics*, 170(9), 1369–1384. doi: 10.1007/s00024-012-0477-5
- Nakamura, T., Takenaka, H., Okamoto, T., & Kaneda, Y. (2012). FDM simulation of seismic-wave propagation for an aftershock of the 2009 Suruga Bay earthquake: Effects of ocean-bottom topography and seawater layer. *Bulletin of the Seismological Society of America*, 102(6), 2420–2435. doi: 10.1785/0120110356
- Noguchi, S., Maeda, T., & Furumura, T. (2016). Ocean-influenced Rayleigh waves from outer-rise earthquakes and their effects on durations of long-period ground motion. *Geophysical Journal International*, 205(2), 1099–1107. doi: 10.1093/gji/ggw074
- Oeser, J., Bunge, H. P., & Mohr, M. (2006). Cluster design in the Earth Sciences Tethys. *Lecture Notes in Computer Science (including subseries Lecture Notes in Artificial Intelligence and Lecture Notes in Bioinformatics)*, 4208 LNCS, 31–40. doi: 10.1007/11847366\_4
- Olsen, K. B., Madariaga, R., & Archuleta, R. J. (1997). Three-dimensional dynamic simulation of the 1992 Landers earthquake. *Science*, 278(5339), 834–838. doi: 10.1126/SCIENCE.278.5339.834
- Pelties, C., Gabriel, A.-A., & Ampuero, J.-P. (2014). Verification of an ADER-DG method for complex dynamic rupture problems. *Geoscientific Model Development*, 7(3), 847–866. doi: 10.5194/gmd-7-847-2014
- Pukelsheim, F. (2006). *Optimal Design of Experiments*. SIAM. doi: 10.1137/1.9780898719109
- Ragon, T., Sladen, A., & Simons, M. (2018). Accounting for uncertain fault geometry in earthquake source inversions – I: Theory and simplified application. *Geophysical Journal International*, 214(2), 1174–1190. doi: 10.1093/gji/ggy187
- Ramos, M. D., Huang, Y., Ulrich, T., Li, D., Gabriel, A. A., & Thomas, A. M. (2021). Assessing margin-wide rupture behaviors along the Cascadia megathrust with 3-D dynamic rupture simulations. *Journal of Geophysical Research: Solid Earth*, 126(7), e2021JB022005. doi: 10.1029/2021JB022005
- Ramos, M. D., Thakur, P., Huang, Y., Harris, R. A., & Ryan, K. J. (2022). Working with dynamic earthquake rupture models: A practical guide. *Seismological Research Letters*, 93(4), 2096–2110. doi: 10.1785/0220220022
- Saito, T., Baba, T., Inazu, D., Takemura, S., & Fukuyama, E. (2019). Synthesizing sea surface height change including seismic waves and tsunami using a dynamic rupture scenario of anticipated Nankai Trough earthquakes. *Tectonophysics*, 769, 228166.
- Salaree, A., Huang, Y., Ramos, M. D., & Stein, S. (2021). Relative tsunami hazard from segments of Cascadia Subduction Zone for Mw 7.5–9.2 earthquakes. *Geophysical Research Letters*, 48(16), e2021GL094174. doi: 10.1029/2021GL094174

- Sallarès, V., & Ranero, C. R. (2019). Upper-plate rigidity determines depth-varying rupture behaviour of megathrust earthquakes. *Nature*, *576*(7785), 96–101. doi: 10.1038/s41586-019-1784-0
- Satake, K., Wang, K., & Atwater, B. F. (2003). Fault slip and seismic moment of the 1700 Cascadia earthquake inferred from Japanese tsunami descriptions. *Journal of Geophysical Research: Solid Earth*, *108*(B11). doi: 10.1029/2003JB002521
- Saunders, J. K., & Haase, J. S. (2018). Augmenting onshore GNSS displacements with offshore observations to improve slip characterization for Cascadia Subduction Zone earthquakes. *Geophysical Research Letters*, *45*(12), 6008–6017. doi: 10.1029/2018GL078233
- Schindelé, F., Kong, L., Lane, E. M., Paris, R., Ripepe, M., Titov, V., & Bailey, R. (2024). A review of tsunamis generated by volcanoes (TGV) source mechanism, modelling, monitoring and warning systems. *Pure and Applied Geophysics*, *181*(6), 1745–1792.
- Schmidt, D., Wilcock, W., LeVeque, R. J., Gonzalez, F., Cram, G., Manalang, D., ... Bodin, P. (2019). *Earthquake and tsunami early warning on the Cascadia subduction zone: A feasibility study for an offshore geophysical monitoring network* (Tech. Rep.). University of Washington. (<https://hdl.handle.net/1773/50968>)
- Schulten, I., Mosher, D. C., Piper, D. J. W., & Krastel, S. (2019). A massive slump on the St. Pierre Slope, a new perspective on the 1929 Grand Banks submarine landslide. *Journal of Geophysical Research: Solid Earth*, *124*(8), 7538–7561. doi: 10.1029/2018JB017066
- Small, D. T., Melgar, D., La Selle, S., & Meigs, A. (2025). Combining multisite tsunami and deformation modeling to constrain slip distributions for the 1700 C.E. Cascadia earthquake. *Bulletin of the Seismological Society of America*, *115*(2), 431–451. doi: 10.1785/0120240218
- Stanzione, D., West, J., Evans, R. T., Minyard, T., Ghattas, O., & Panda, D. K. (2020). Frontera: The evolution of leadership computing at the National Science Foundation. In *Practice and Experience in Advanced Research Computing 2020: Catch the Wave* (pp. 106–111). Association for Computing Machinery. doi: 10.1145/3311790.3396656
- Stuart, A. M. (2010). Inverse problems: A Bayesian perspective. *Acta Numerica*, *19*, 451–559. doi: 10.1017/S0962492910000061
- Svennevig, K., Hicks, S. P., Forbriger, T., Lecocq, T., Widmer-Schmidrig, R., Mangeney, A., ... Wirtz, B. (2024). A rockslide-generated tsunami in a Greenland fjord rang Earth for 9 days. *Science*, *385*(6714), 1196–1205. doi: 10.1126/science.adm9247
- Tang, L., Titov, V. V., Moore, C., & Wei, Y. (2017). Real-time assessment of the 16 September 2015 Chile tsunami and implications for near-field forecast. In C. Braitenberg & A. B. Rabinovich (Eds.), *The Chile-2015 (Illapel) Earthquake and Tsunami* (pp. 267–285). Springer International Publishing. doi: 10.1007/978-3-319-57822-4\_19
- Tanioka, Y., & Gusman, A. R. (2018). Near-field tsunami inundation forecast method assimilating ocean bottom pressure data: A synthetic test for the 2011 Tohoku-Oki tsunami. *Physics of the Earth and Planetary Interiors*, *283*, 82–91. doi: 10.1016/j.pepi.2018.08.006
- Tsushima, H., Hino, R., Fujimoto, H., Tanioka, Y., & Imamura, F. (2009). Near-field tsunami forecasting from cabled ocean bottom pressure data. *Journal of Geophysical Research: Solid Earth*, *114*(B6). doi: 10.1029/2008JB005988
- Tu, J., Karlin, I., Camier, J., Dobrev, V., Kolev, T., Henneking, S., & Ghattas, O. (2026). Accelerating high-order finite element simulations at extreme scale with FP64 tensor cores. *arXiv:2603.09038*. doi: 10.48550/arXiv.2603.09038
- Ulrich, T., Gabriel, A. A., & Madden, E. H. (2022). Stress, rigidity and sediment strength control megathrust earthquake and tsunami dynamics. *Nature Geoscience*, *15*(1), 67–73. doi: 10.1038/s41561-021-00863-5
- Uphoff, C., Rettenberger, S., Bader, M., Madden, E. H., Ulrich, T., Wollherr, S., & Gabriel, A.-A. (2017). Extreme scale multi-physics simulations of the tsunamigenic 2004 Sumatra megathrust earthquake. In *Proceedings of the International Conference for High Performance Computing, Networking, Storage and Analysis* (pp. 1–16). ACM. doi: 10.1145/3126908.3126948

- van Zelst, I., Rannabauer, L., Gabriel, A. A., & van Dinther, Y. (2022). Earthquake Rupture on Multiple Splay Faults and Its Effect on Tsunamis. *Journal of Geophysical Research: Solid Earth*, *127*(8), e2022JB024300. doi: 10.1029/2022JB024300
- Venkat, S., Fernando, M., Henneking, S., & Ghattas, O. (2025). Fast and scalable FFT-based GPU-accelerated algorithms for block-triangular Toeplitz matrices with application to linear inverse problems governed by autonomous dynamical systems. *SIAM Journal on Scientific Computing*, *47*(5), B1201–B1226. doi: 10.1137/24M1683172
- Walton, M. A. L., Staisch, L. M., Dura, T., Pearl, J. K., Sherrod, B., Gomberg, J., ... Wirth, E. (2021). Toward an integrative geological and geophysical view of Cascadia Subduction Zone earthquakes. *Annual Review of Earth and Planetary Sciences*, *49*(Volume 49, 2021), 367–398. doi: 10.1146/annurev-earth-071620-065605
- Wang, P.-L., Engelhart, S. E., Wang, K., Hawkes, A. D., Horton, B. P., Nelson, A. R., & Witter, R. C. (2013). Heterogeneous rupture in the great Cascadia earthquake of 1700 inferred from coastal subsidence estimates. *Journal of Geophysical Research: Solid Earth*, *118*(5), 2460–2473. doi: 10.1002/jgrb.50101
- Wei, Y., Bernard, E. N., Tang, L., Weiss, R., Titov, V. V., Moore, C., ... Kânoğlu, U. (2008). Real-time experimental forecast of the Peruvian tsunami of August 2007 for U.S. coastlines. *Geophysical Research Letters*, *35*(4). doi: 10.1029/2007GL032250
- Wendt, J., Oglesby, D. D., & Geist, E. L. (2009). Tsunamis and splay fault dynamics. *Geophysical Research Letters*, *36*(15). doi: 10.1029/2009GL038295
- Williamson, A. L., Melgar, D., Crowell, B. W., Arcas, D., Melbourne, T. I., Wei, Y., & Kwong, K. (2020). Toward near-field tsunami forecasting along the Cascadia Subduction Zone using rapid GNSS source models. *Journal of Geophysical Research: Solid Earth*, *125*(8), e2020JB019636. doi: 10.1029/2020JB019636
- Wilson, A., & Ma, S. (2021). Wedge plasticity and fully coupled simulations of dynamic rupture and tsunami in the Cascadia Subduction Zone. *Journal of Geophysical Research: Solid Earth*, *126*(7), e2020JB021627. doi: 10.1029/2020JB021627
- Wirp, S. A., Kutschera, F., Gabriel, A.-A., Ulrich, T., Bader, M., & Lorito, S. (2025). *Hellenic Arc tsunami generation from Mw8+ 3D margin-wide dynamic rupture earthquake scenarios* (No. 10.31223/X52X6M). EarthArXiv. doi: 10.31223/X52X6M
- Wirth, E. A., Frankel, A. D., Sherrod, B., Grant, A. R., Dunham, A., Stone, I. P., & Grossman, J. (2025). Earthquake probabilities and hazards in the U.S. Pacific Northwest. *U.S. Geological Survey Fact Sheet 2025–3050*, 6. doi: 10.3133/fs20253050
- Wong, J. W. C., Gabriel, A.-A., & Fan, W. (2026). *Dynamic restrengthening and fault heterogeneity explain megathrust earthquake complexity* (No. arXiv:2505.08973). arXiv. doi: 10.48550/arXiv.2505.08973
- Wu, K., Chen, P., & Ghattas, O. (2023). An offline-online decomposition method for efficient linear Bayesian goal-oriented optimal experimental design: Application to optimal sensor placement. *SIAM Journal on Scientific Computing*, *45*(1), B57–B77. doi: 10.1137/21M1466542

## SUPPORTING INFORMATION

### Contents of this file

1. Text S1
2. Table S1
3. Figures S1 to S3

### **Text S1: 3D fully-coupled earthquake dynamic rupture–tsunami simulations**

To model both 3D fully-coupled earthquake dynamic rupture and tsunami scenarios used in this study, we use SeisSol which is based on the Arbitrary high-order DERivative-Discontinuous Galerkin (ADER-DG) method (Käser & Dumbser, 2006; Dumbser & Käser, 2006). SeisSol has been verified against a set of community benchmark problems, including a recent 3D fully-coupled setup (e.g., Pelties et al., 2014; Harris et al., 2018; Kutschera et al., 2025), and has been optimized for high-performance computing (e.g., Uphoff et al., 2017). We use SeisSol with sixth-order accuracy in time and space (i.e., polynomial order of  $p = 5$ ) and simulate 420 s of earthquake–tsunami generation. Both fully-coupled simulations were run on the *Frontera* supercomputer (Stanzione et al., 2020) using 102 nodes (5,712 cores), each requiring about 175 kCPUh.

The fully-coupled simulations required a modification to the unstructured tetrahedral mesh of Glehman et al. (2025), incorporating the ocean acoustic water layer atop the elastic domain (solid Earth). Thus, we rebuild the 3D unstructured, tetrahedral mesh with the same 1.5 km on-fault mesh resolution (Glehman et al., 2025) and a resolution of 0.4 km in the acoustic medium. The resulting mesh is composed of a total of 103,386,944 elements. Out of those, 43,633,138 elements represent the solid Earth and 59,753,806 elements the water layer.

We note that the modeling domain for the ocean acoustic water layer in our fully-coupled simulations is spatially limited and involves sharp bends due to the high computational cost and the non-trivial intersection of the water layer with the coast (Wirp et al., 2025). Thus, along the edges, the faster-propagating seismo-acoustic waves may be reflected in the E–W direction, as the width of the water layer is shorter compared to its length. However, the amplitudes of those boundary reflections are  $\sim 80\%$  smaller compared to the physically generated seismo-acoustic waves and  $\sim 99\%$  smaller than the peak tsunami amplitude (Supporting Information, Movie S3).

Properties of the margin-wide and partial dynamic rupture scenario are listed in Supporting Information, Table S1. This expands on the reported rupture duration, peak slip rate, ruptured area, estimated stress drop, and the peak vertical ground displacements of the dynamic rupture scenarios given in Glehman et al. (2025).

**Table 1.** Dynamic rupture parameters and key results for the two fully-coupled dynamic rupture scenarios expanded from (Glehman et al., 2025). \*Considering those parts of the fault where the slip exceeds 0.2 m.

	Partial rupture	Margin-wide rupture
Glehman et al. (2025)	Model 2	Model 16
Static friction coefficient ( $\mu_s$ )	0.6	0.6
Dynamic friction coefficient ( $\mu_d$ )	0.1	0.1
Critical slip-weakening distance ( $D_c$ ) [m]	1.0	1.0
Nucleation radius ( $r_{crit}$ ) [km]	3400	4400
Nucleation depth [km]	16	16
Pore fluid ratio ( $\gamma$ )	0.97	0.97
Moment magnitude $M_W$	8.6	8.7
Rupture duration [s]	$\sim 140$	$\sim 270$
Peak slip rate [ $\text{m s}^{-1}$ ]	2.26	2.37
Peak slip [m]	11.25	11.34
Average slip [m]*	$\sim 4.9$	$\sim 4.8$
Ruptured area [ $\text{km}^2$ ]*	58,349.6	86,767.3
Stress drop [MPa]*	1.33	1.45
Peak seafloor uplift (final) [m]	1.59	1.69
Peak seafloor subsidence (final) [m]	-2.03	-2.07

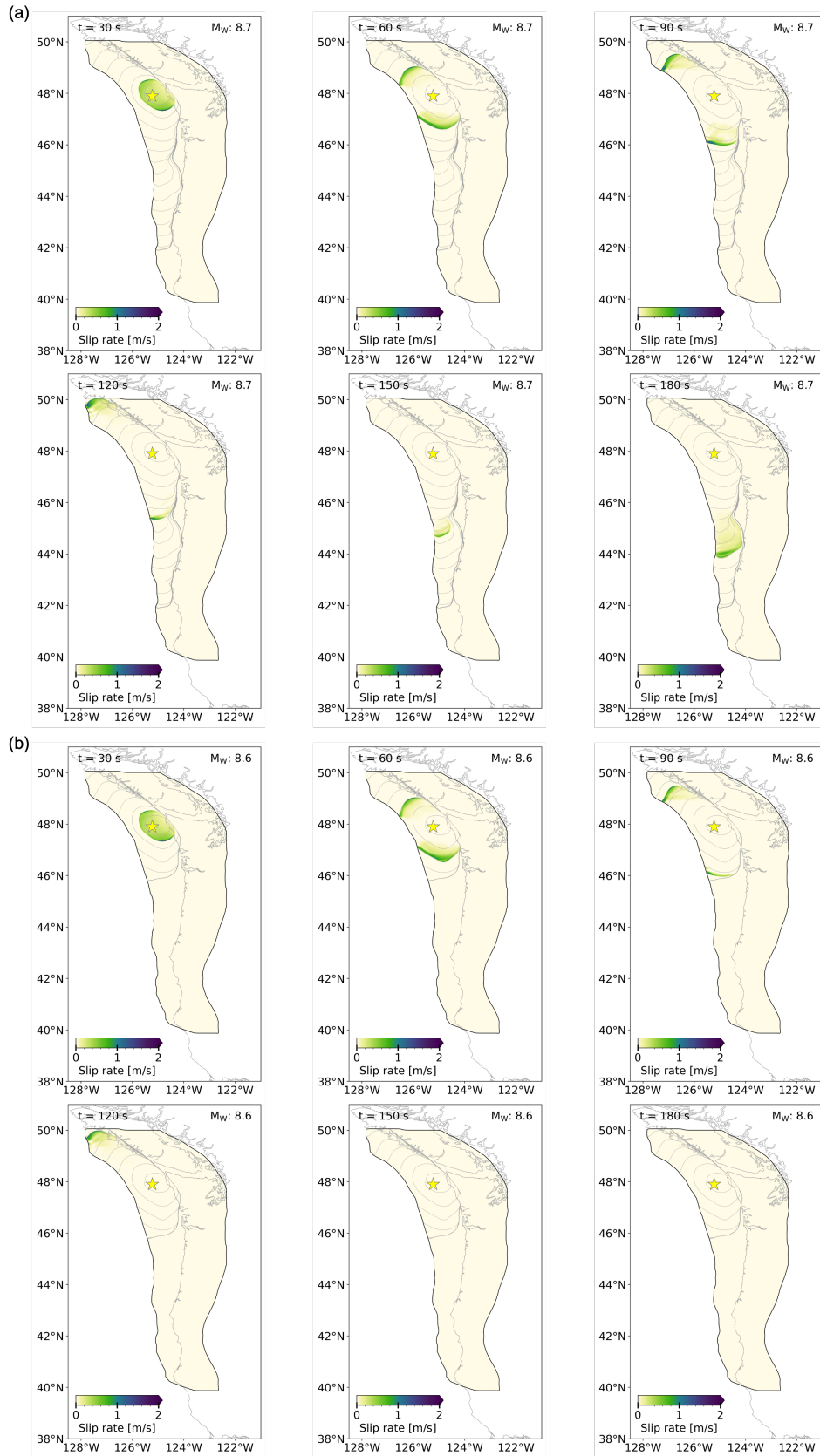


**Figure 4.** Snapshots of the slip rate every 30 s for (a) the margin-wide rupture and (b) the partial rupture scenario. The respective final moment magnitude is annotated at the top right. Note the earlier rupture arrest for the partial rupture scenario compared to the margin-wide rupture. Animations of the slip rate are uploaded as additional, supplementary movies.

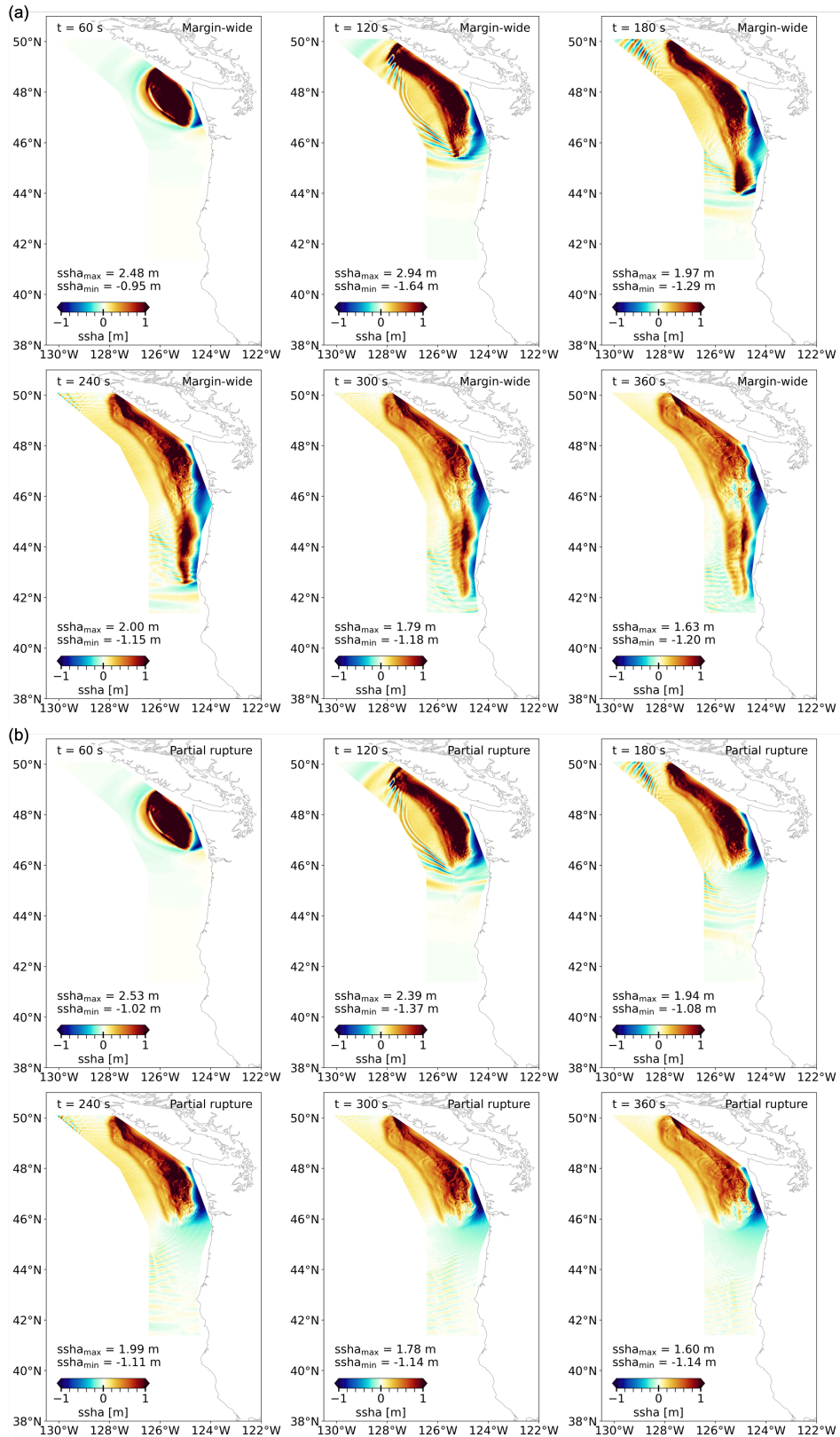


**Figure 5.** Snapshots of the seismo-acoustic and gravity wave (i.e., tsunami) excitation at the sea surface as indicated by the sea surface height anomaly (ssha) every 60 s for (a) the margin-wide rupture and (b) the partial rupture scenario. Animations of the time-dependent ssha are uploaded as additional, supplementary movies.

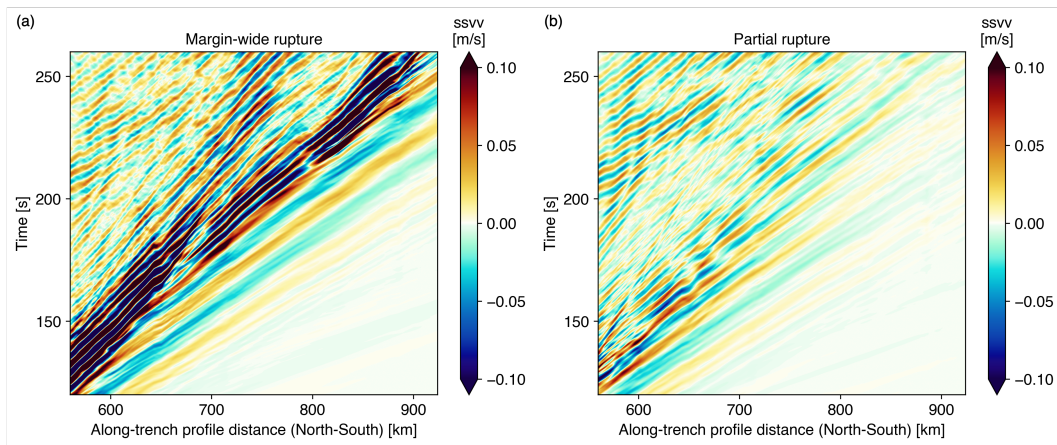


**Figure 6.** Zoom into the space-time evolution of the sea surface vertical velocities (ssvv) for (a) the margin-wide rupture and (b) the partial rupture scenario, showing the attenuating oceanic Rayleigh waves once the partial rupture has arrested in comparison to the ongoing margin-wide rupture scenario.